IRANIAN JOURNAL OF PHYSICS RESEARCH

Iranian Journal of Physics Research, Vol. 3. No. 2, 2002

Review article

The nano-science of C_{60} molecule

H Rafii-Tabar

Computational Physical Sciences Laboratory, School of Physics, Institute for Studies in Theoretical Physics and Mathematics (IPM), P. O. Box 19395-5531, Tehran

(Received 4 March 2002; accepted 8 May 2002)

Abstract

Over the past few years, nano-science and its associated nano-technology have emerged into prominence in research institutions across the world. They have brought about new scientific and engineering paradigms, allowing for the manipulation of single atoms and molecules, designing and fabricating new materials, atom-by-atom, and devices that operate on significantly reduced time and length scales. One important area of research in nano-science and nano-technology is carbon-based physics in the form of fullerene physics. The C_{60} molecule, and other cage-like fullerenes, together with carbon nanotubes provide objects that can be combined to generate three-dimensional functional structures for use in the anticipated nano-technology of future. The unique properties of C_{60} can also be exploited in designing nano-phase thin films with applications in nanoscopic device technology and processes such as nano-lithography. This requires a deep understanding of the highly complex process of adsorption of this molecule on a variety of substrates. We review the field of nano-scale nucleation and growth of C_{60} molecules on some of the technologically important substrates. In addition to experimental results, the results of a set of highly accurate computational simulations are also reported.

Keywords: nano-science, nano-technology, nano-phase films, nano-scale modelling, MD simulations, nano-science of C_{60}, C_{60}/Si, C_{60}/graphite

1. Introduction

Nano-science and nano-technology [1, 2, 3, 4] form two basic pathways in research concerned with *purposeful* manipulation and structural transformation of condensed phases at their most fundamental levels. They allow us to exercise a complete control over the structure and functioning of physical matter at the atomistic and molecular scales. This control implies that physical matter can be interrogated atom-by atom and molecule-by-molecule and new types of materials can be designed from bottom-up, atom-by-atom, by a precise positioning of individual atoms and molecules, leading to the formation of phases with fundamentally different properties and functions than the existing micro-scale, or macro-scale, phases.

Matter at nanoscopic scales and matter composed of nano-scale grains, the so-called nano-phase matter, have properties that are significantly different from the ordinary coarse-grained matter. For example, a number of studies have shown that nano-structured metallic materials with average grain sizes between 5 and 50 nanometres exhibit very unique properties. In particular, it is known that these materials have much improved mechanical properties compared with their coarse-grained counterparts [5, 6]. For example, the dense nano-structured Ni and Ni alloys show an increase in strength by factors from 3 to 10 and in hardness by a factor of 5, and an enhancement in wear resistance by up to 170 times the normal coarse-grained materials [7].

The fundamental entities which nano-science and nano-technology are concerned with are the *nano-*

structures. These are constructed from *countable* number of atoms, or molecules, and are intermediate in size between molecules and micro-structures. One of their characteristic features is their high surface-to-volume ratio. Their electronic and magnetic properties are often distinguished by quantum mechanical behaviour, while their mechanical and thermal properties can be understood within the framework of classical statistical mechanics. Nano-structures can appear in all forms of condensed matter, be it soft or hard, biological or non-biological, ordered or disordered. Accordingly, nano-science and nano-technology have been specialised into several distinct areas, namely the *wet* nano-technology, the *dry* nano-technology and the *computational* nano-technology. The wet nano-technology is mainly concerned with the study of nano-structures and nano-processes in biological systems that live in aqueous environment. The functional nano-structures in this field are bio-materials, genetic materials, bio-membranes, enzymes and many other cellular components. There is no doubt that, biological systems offer an excellent example of functioning nano-structures. Dry nano-technology, on the other hand, is based on surface science and physical chemistry. The focus of this technology is on metallic, semi-metallic and semi-conducing materials. The electronic structure of these materials provides a favourable framework for constructing nano-structures that can be used in electronic, magnetic and optical devices.

Computational nano-technology, in the form of numerical modelling and computer-based simulation, is based on computational condensed matter physics and materials modelling [8]. Its domain covers both aspects of nano-technology, and by employing concepts from both classical physics and quantum-mechanical many body theories, it investigates the properties of nano-structures and nano-processes, their formation and evolution, atom-by-atom, via precise numerical experiments on any form of condensed phases.

The emergence of gigantic computational facilities, in the form of super-computers, graphic workstations and powerful personal computers, has led to the formation of a new science, referred to as the *Computational Science*, forming the Third Branch of research along side the traditional theory-building and laboratory-based experimentation. Computational science consists of numerical modelling and computer-based simulation of condensed phases at the macro-, meso- and nano-scales, and, recently, their integration into unified *multi-scale* models of phenomena in which a complete description requires the coupling of many processes at widely different length, time and energy scales. At the nano-scale, the aim of the computational science is to study the evolution of physical, chemical and biological systems on significantly reduced time and length scales. Numerical simulations implemented at the this scale form the basis of computational nano-technology. These simulations allow for an understanding of the atomistic mechanisms, energetics and dynamics underlying the physical processes that can unfold in isolated and interacting nano-structures under different conditions. Numerical simulations are based on large-scale codes that can be implemented on various types of computing platforms. The implementation of such codes constitutes a kind of computational experimentation for testing the model system for a variety of initial and environmental parameters. In simulations, we have a complete control over all the forces that may influence the structure and properties of the nano-structure under study. The effects of physical parameters on the system can be precisely isolated and systematically studied. Computational simulations can be used to provide exhaustive accounts of the logical consequences that emanate from specific assumptions, input data and the physical theories underlying the energetics and dynamics of the model system. Therefore, simulations provide a comprehensive knowledge about the condensed phases at a level that can not be obtained in other ways. From this perspective, simulations can provide the research scientists with unforseen and totally unexpected scenarios.

Computational nano-science, in the form of nano-scale modelling [8], together with experimental nano-science, employing *tip-based* probe techniques, such as scanning tunnelling microscopy (STM) [9] and atomic force microscopy (AFM) [10], have generated new and exciting fields of research, closely aligned to the field of nano-technology, such as nano-mechanics, nano-optics, nano-magnetism and nano-electronics. These tip-based devices have provided revolutionary tools for a nanoscopic interrogation of the morphology and electronic structure maps of material surfaces and have made their atomic-scale manipulation possible. Probe-based techniques have been further extended and are

now collectively referred to as the scanning probe microscopy (SPM).

This review is concerned with one of the most important areas of the current research in nano-science and nano-technology, i.e. the field of fullerene-based physics, and in particular the nano-science of the C_{60} molecule, which continues to occupy a prominent place in research activities in the field of computational and experimental nano-science across the world. The review is mainly based on the research which the author has been associated with in the field of computational nano-science of C_{60}. The organisation of this paper is as follows. In Section 2, one of the modelling tools of the computational nano-science , and the one employed in the simulations reported here, is briefly described. This is followed , in Section 3, by a description of the pertinent inter-atomic potentials that model the energetics and dynamics of the processes involved in the adsorption of this molecule on a variety of substrates. We then briefly review, in Section 4, the main results from some of the experiments performed on the adsorption of C_{60} molecules on a variety of metallic surfaces. Section 5 is devoted to the description of the computational simulations of the adsorption of C_{60} molecules on semi-conducting and semi-metallic surfaces.

2. Molecular dynamics (MD) modelling of a canonical ensemble

2.1 Basic notions

Computational simulations at nanoscopic scales are performed through several distinct methodologies. The most widely used in modelling the nano-structures and nano-processes in condensed matter physics and the related field of materials modelling is the *dynamic* approach known as the molecular dynamics (MD) simulation method [11, 12, 13] where the motion of individual atoms, within an assembly of N atoms, or molecules, in any type of condensed phase, is modelled on the basis of either a Newtonian deterministic dynamics or a Langevin-type stochastic dynamics, given their initial position coordinates and velocities. A classical MD simulation proceeds by constructing a finite *nano-sized* portion, say N atoms, of an infinite model system with any desired configuration in either a crystalline or an amorphous state in a primary computational cell of volume V. The cell is replicated in all spatial dimensions generating its own periodic images as well as those of the original N atoms. This is called the periodic boundary condition (PBC), and is introduced to remove the undesirable effects of the artificial surfaces associated with the finite size of the simulated system.

The energetics and dynamics of the atoms are obtained from prescribed two-body and many-body *phenomenological* inter-atomic potentials, $H_I(r_{ij})$, from which the Newtonian forces experienced by these atoms are derived via

$$\mathbf{F}_i = -\sum_{j>i} \nabla_{r_i} H_I(r_{ij}), \tag{1}$$

The $3N$ position degrees of freedom set up $3N$ simultaneous coupled differential equations of motion which are integrated numerically within the computational cell by a variety of finite-difference techniques, among which the most frequently used is the velocity Verlet algorithm [11]. According to this algorithm, the positions, $\mathbf{r}_i$, and velocities, $\mathbf{v}_i$, of the atoms of mass m_i are updated at each simulation time step, dt, by

$$\mathbf{r}_i(t+dt) = \mathbf{r}_i(t) + v_i(t)dt + \frac{1}{2}dt^2\,\frac{\mathbf{F}_i(t)}{m_i},$$

$$\mathbf{v}_i(t+\frac{1}{2}dt) = \mathbf{v}_i(t) + \frac{1}{2}dt\,\frac{\mathbf{F}_i(t)}{m_i},$$

$$\mathbf{v}_i(t+dt) = \mathbf{v}_i(t+\frac{1}{2}dt) + \frac{1}{2}dt\,\frac{\mathbf{F}_i(t+dt)}{m_i} \tag{2}$$

When the original N atoms move in the primary cell, their periodic images execute exactly identical motion in their respective image cells. When one atom leaves the primary cell from one side, one of its periodic images enters from the opposite side via the PBC, thus keeping the number of particles constant. The dynamical history of a particular micro-state of the system, constructed initially, can therefore be followed by computing the space-time *trajectories* through the phase space via eqs. (2). At each instant of the simulation time, the exact instantaneous values of the observables, such as pressure, temperature and thermodynamics response functions, are also obtained, leading to time-average values at the conclusion of the simulation.

2.2 Nose-Hoover dynamics

The behaviour of a system with a fixed number of atoms, N, confined to a fixed volume, V, and maintained at a

constant preset temperature, *T*, is studied within the framework of a constant-(NVT), or a *canonical*, ensemble [14], with the temperature acting as a *control* parameter.

A constant-temperature MD simulation can be realised in a variety of ways. The earliest proposal [15, 16] consisted of a simple *constraint* method to restrict the total kinetic energy of the system in order to maintain a reference temperature. This was done by a simple re-scaling of the particle velocities at each simulation time step in order to correct for the thermal drift. No rigorous proof was, however, advanced to justify this method, or show that it leads to the generation of a constant-(NVT) ensemble. An early application of this method to an exactly solvable problem consisting of 3200 coupled harmonic oscillators [17] showed that it had a negligible effect on the dynamical properties of the system. The method was modified [18] by constraining the kinetic energy via a momentum scaling. However, it was shown [19] that in an N-particle system, this momentum scaling method produces an equilibrium distribution function which deviates from a canonical distribution by an order of $N^{-\frac{1}{2}}$.

A second proposal to realise a constant temperature ensemble was based on a *stochastic*, Langevin-type, method [20, 21, 22]. This is essentially a hybrid method that combines the MD and Monte Carlo techniques. In this method the particle velocities are modified during stochastic collisions with some form of ghost particles. These collisions reset the particle velocities to new values and establish a balance between randomized thermal agitations and a frictional force, leading to the generation of a canonical distribution. The method was applied to the simulation of a water system [23] and it was found that in order to realise a constant temperature the frequency of random collisions must be selected from a certain range. A rapid collision rate would lead to the loss of short-time memory by the particles and the rapid dissipation of the long-time auto-correlation function. Hence, these collisions must take place with low frequency.

A second constraint method, based on the techniques of non-equilibrium MD, was also proposed [24, 25, 26] in which an additional term, proportional to the momenta of the particles, is added to the force terms in the equations of the motion. This addition makes these equations no longer of a canonical form. The constant of proportionality is then determined so as to produce a constant total kinetic energy. This method generates a canonical distribution only in the configuration space part of the phase space if the number of degrees of freedom of an *N*-particle system is set to (3N-1) rather than to 3N. It has been pointed out that [27] this new constraint method has two drawbacks. Firstly, since the reference temperature does not appear explicitly in the equations, then any inaccuracy of the algorithm can lead to an instability in the value of the temperature. Secondly, the Hamiltonian of the method does not correspond to a physical system, and therefore the introduction of a non-physical Hamiltonian may be objectionable, on physical grounds, for simulations of physical systems even though this Hamiltonian produces consistent equations of motion on mathematical grounds.

In addition to these constraint and stochastic methods, a new method that generates the canonical ensemble distribution in *both* the configuration space and momentum space parts of the phase space was proposed by Nose' [19, 28, 29] and Hoover [30] and is referred to as the *extended system* method. The method is quite rigorous and more general than the second constraint method discussed above since that method produces a canonical distribution in the configuration space alone. In fact it was demonstrated [19] that the equations of the second constraint method can be obtained from this extended method. The extended system method is therefore the approach that we adopted for constructing the canonical ensembles used in our simulations. Before we discuss the details of this method, let us first remark that in statistical mechanics, a representative canonical ensemble can be constructed by taking a large number of systems, that are mental replicas of the physical system, each of volume V and containing N atoms, and stack them together to form a three-dimensional block (ensemble). The block is then placed in a heat bath at temperature T. If we assume that the boundaries separating the members of this block are only permeable to the exchange of energy, and not matter, then when the members of the block have equilibrated with the bath, they all attain a common temperature T. If such a block is then thermally insulated it forms a canonical ensemble. In this method, an amount of energy, the energy of the bath, is shared by the members of the ensemble and the statistics involved is

that of this sharing process. An equivalent procedure would be to consider the system as in equilibrium with an external heat bath at a common temperature T. The system and the bath exchange no particles but only energy. Since there is a thermal contact between the two, the total energy of the system fluctuates and its equilibrium distribution approaches that of a canonical ensemble. In this method, the statistics involved is that of this energy exchange between the system and the bath.

According to the extended system method, the simulated system and the heat bath couple to form a composite system. The coupling breaks the energy conservation that restricts the behaviour of the simulated system and leads to a canonical ensemble. The conservation of energy still holds in the composite system, but the total energy of the simulated system is allowed to fluctuate.

The scheme furnishes a continuous deterministic dynamics. It is based on the extension of the space of dynamical variables of the system beyond that of the coordinates and momenta of the *real* particles to include one additional *phantom* coordinate, s, and its conjugate momentum, p_s, [31]. If these coordinates are appended to the system, it is then referred to as the extended system. This extra degree of freedom acts as a heat bath for the real particles. There are, therefore, four systems to consider, namely, the real ($\mathbf{r}_i$, $\mathbf{p}_i$) system, the virtual ($\tilde{\mathbf{r}}_i, \tilde{\mathbf{p}}_i$) system, the real extended ($\mathbf{r}_i$, $\mathbf{p}_i$, s, p_s) system and the virtual extended ($\tilde{\mathbf{r}}_i, \tilde{\mathbf{p}}_i, s, p_s$) system. The aim of the Nose's approach is to show that there is a method for selecting the Hamiltonian of the extended system and, simultaneously, to relate the variables of the real physical system to those of the virtual system, such that *the micro-canonical partition function of the extended virtual system is proportional to the canonical partition function of the real physical system* [31].

The Hamiltonian of the virtual extended system is

$$H^* = \sum_i^N \frac{\tilde{\mathbf{p}}_i^2}{2m_i s^2} + H_I(\tilde{r}_{ij}) + \frac{p_s^2}{2Q} + gk_B T \ln s, \qquad (3)$$

where g is the number of degrees of freedom, k_B is the Boltzmann constant, Q is a parameter which behaves like a `mass' associated with the motion of the coordinate s, and $\mathbf{r}_i$, $\mathbf{p}_i$, $\tilde{\mathbf{r}}_i$ and $\tilde{\mathbf{p}}_i$ are the canonical position and momentum coordinates of all the particles in the real and virtual systems. The virtual coordinates, and the time, are related to the corresponding real physical coordinates via the transformations

$$\mathbf{r}_i = \tilde{\mathbf{r}}_i$$

$$\mathbf{p}_i = \frac{1}{s}\tilde{\mathbf{p}}_i$$

$$dt = \frac{1}{s}d\tilde{t}. \qquad (4)$$

Since H_I in eq. (3) is the potential energy for both the real and virtual systems, then the first two terms in eq. (3) represent the kinetic and potential energies of the physical system, and the last two terms correspond to the kinetic and potential energies associated with the extra degree of freedom.

From this Hamiltonian, the equations of motion of the physical system are obtained

$$\frac{d\mathbf{r}_i}{dt} = \frac{\mathbf{p}_i}{m_i},$$

$$\frac{d\mathbf{p}_i}{dt} = \mathbf{F}_i - \eta\mathbf{p}_i,$$

$$\frac{d\eta}{dt} = \frac{1}{Q}\left(\sum_i \frac{\mathbf{p}_i^2}{m_i} - gk_B T\right), \qquad (5)$$

where η is called the friction coefficient of the bath. This coefficient is not a constant and can take on both positive and negative values. This gives rise to what is called a *negative feedback mechanism*. The last equation in (5) controls the functioning of the heat bath. From this equation we observe that if the total kinetic energy is greater than $gk_BT/2$ then $d\eta/dt$, and hence η, is positive. This prompts a friction inside the bath and correspondingly the motion of the atoms are decelerated to lower their kinetic energy to that of the bath. On the other hand, if the kinetic energy is lower than $gk_BT/2$, then $d\eta/dt$ will be negative, and this results in the bath being heated up and accelerate the motion of the atoms. Equations (5) are collectively referred to as the Nose'-Hoover *thermostat*.

2.3 Equations of motion

The realisation of a canonical ensemble via Nose'-Hoover dynamics leads to a modification of equations of motion (2). A velocity Verlet formulation of the equations of motion in this dynamics can be given [32]

$$\mathbf{r}_i(t+dt) = \mathbf{r}_i(t) + \mathbf{v}_i(t)dt + \frac{1}{2}dt^2\left[\frac{\mathbf{F}_i(t)}{m_i} - \eta(t)\mathbf{v}_i(t)\right],$$

$$\mathbf{v}_i(t+\frac{dt}{2}) = \mathbf{v}_i(t) + \frac{dt}{2}\left[\frac{\mathbf{F}_i(t)}{m_i} - \eta(t)\mathbf{v}_i(t)\right],$$

$$\eta(t+\frac{dt}{2}) = \eta(t) + \frac{dt}{2Q}\left[\sum_i^N m_i v_i^2(t) - gk_BT\right],$$

$$\eta(t+dt) = \eta(t+\frac{dt}{2}) + \frac{dt}{2Q}\left[\sum_i^N m_i v_i^2(t+\frac{dt}{2}) - gk_BT\right],$$

$$\mathbf{v}_i(t+dt) = \frac{2}{2+\eta(t+dt)dt}\left[\mathbf{v}_i(t+\frac{dt}{2}) + dt\frac{\mathbf{F}_i(t+dt)}{2m_i}\right]. \quad (6)$$

A particular parameterization of the Q is given by

$$Q = gk_BT\tau^2, \quad (7)$$

where τ is the relaxation time of the heat bath, normally of the same order of magnitude as the simulation time step, dt. It controls the speed with which the bath damps down the fluctuations in the temperature. The number of degrees of freedom is given by g=3(N-1).

3. Inter-atomic potentials

The use of phenomenological inter-atomic potentials to model the energetics and dynamics of nano-structures lies at the very foundation of the computer-based MD simulations. These potentials contain the *physics* of the model systems. The significance of much of the simulation results, their accuracy and the extent to which they represent the real behaviour of condensed phases, and their transitions, under varied conditions depends in a critical manner on a realistic choice of a potential energy function. A variety of pair-wise additive and many-body inter-atomic potentials for modelling the physics of different classes of materials, such as metals, non-metals, semi-conductors etc, have been developed [33], and in this section we shall describe those potentials that are directly relevant to the modelling studies reported in this survey.

3.1 Covalently-bonding atom potentials

3.1.1 The Tersoff many-body C-C, Si-Si and C-Si potentials

According to Abell's prescription [34], the binding energy of an atomic many-body system can be computed in terms of pair-wise nearest-neighbour interactions that are, however, modified by the *local* atomic environment. Tersoff employed this prescription to obtain the binding energy in Si [35, 36, 37], C [38], Si-C [37, 39], Ge and Si-Ge [39] solid-state structures.

In the Tersoff's model, the total binding energy is expressed as

$$H_I^{TR} = \sum_i E_i = \frac{1}{2}\sum_i\sum_{j\neq i} V(r_{ij}), \quad (8)$$

wher E_i is the energy of site i and $V(r_{ij})$ is the interaction energy between atoms i and j, given by

$$V(r_{ij}) = f_c(r_{ij})\left[V^R(r_{ij}) + b_{ij}V^A(r_{ij})\right]. \quad (9)$$

The function $V^R(r_{ij})$ represents the repulsive pair-wise potential, such as the core-core interactions, and the function $V^A(r_{ij})$ represents the bonding due to the valence electrons. The many-body feature of the potential is represented by the term b_{ij} which acts as the bond order term and which depends on the local atomic environment in which a particular bond is located. The analytic forms of these potentials are given by

$$V^R(r_{ij}) = A_{ij}e^{-\lambda_{ij}r_{ij}},$$

$$V^A(r_{ij}) = -B_{ij}e^{-\mu_{ij}r_{ij}},$$

$$f_c(r_{ij}) = \begin{cases} 1, & r_{ij} < R_{ij}^{(1)}, \\ \frac{1}{2} + \frac{1}{2}\cos\left[\frac{\pi(r_{ij} - R_{ij}^{(1)})}{(R_{ij}^{(2)} - R_{ij}^{(1)})}\right], & R_{ij}^{(1)} < r_{ij} < R_{ij}^{(2)}, \\ 0, & r_{ij} > R_{ij}^{(2)} \end{cases}$$

$$b_{ij} = \chi_{ij}(1+\beta_i^{n_i}\zeta_{ij}^{n_i})^{-0.5n_i},$$

$$\zeta_{ij} = \sum_{k\neq i,j} f_c(r_{ik})\,\omega_{ik}\,g(\theta_{ijk}),$$

$$g(\theta_{ijk}) = 1 + \frac{c_i^2}{d_i^2} - \frac{c_i^2}{\left[d_i^2 + (h_i - \cos\theta_{ijk})^2\right]},$$

$$\lambda_{ij} = \frac{(\lambda_i + \lambda_j)}{2},\ \mu_{ij} = \frac{(\mu_i + \mu_j)}{2},$$

$$\omega_{ik} = e^{\left[\mu_{ik}^3 (r_{ij} - r_{ik})^3\right]},$$

$$A_{ij} = \sqrt{A_iA_j},\ B_{ij} = \sqrt{B_iB_j},$$

$$R_{ij}^{(1)} = \sqrt{R_i^{(1)}R_j^{(1)}}, R_{ij}^{(2)} = \sqrt{R_i^{(2)}R_j^{(2)}}, \quad (10)$$

Table 1. Parameters of the Tersoff potentials for C and Si.

	C	Si
A(eV)	1.3936×10^{3}	1.8308×10^{3}
B(eV)	3.467×10^{2}	4.7118×10^{2}
$\lambda(\text{A}^{\circ -1})$	3.4879	2.4799
$\mu(\text{A}^{\circ -1})$	2.2119	1.7322
β	1.5724×10^{-7}	1.1000×10^{-6}
n	7.2751×10^{-1}	7.8734×10^{-1}
c	3.8049×10^{4}	1.0039×10^{5}
d	4.384	16.217
h	-0.57058	-0.59825
$R^{(1)}(\text{A}^{\circ})$	1.8	2.7
$R^{(2)}(\text{A}^{\circ})$	2.1	3.0
χ	1	1
χC-Si	0.9776	

where the labels i, j and k refer to the atoms in the ijk bond, r_{ij} and r_{ik} refer to the lengths of the ij and ik bonds whose angle is θ_{ijk}. Singly subscripted parameters, such as λ_i and n_i, depend only on one type of atom, e.g. C or Si. The parameters for the C-C, Si-Si and Si-C potentials are listed in Table 1. For the C, the parameters were obtained by fitting the cohesive energies of carbon polytypes, along with the lattice constant and bulk modulus of diamond. For the Si, the parameters were obtained by fitting to a database consisting of cohesive energies of real and hypothetical bulk polytypes of Si, along with the bulk modulus and bond length in the diamond structure. Furthermore, these potential parameters were required to reproduce all three elastic constants of Si to within 20%.

3.1.2 The Brenner Tersoff-type hydrocarbon potentials

The Tersoff potentials correctly model the dynamics of a variety of solid-state structures, such as the surface reconstruction in Si [35, 36] or the formation of interstitial defects in carbon [38]. However, while these potentials can give a realistic description of the C-C single, double and triple bond lengths and energies in hydrocarbons, solid graphite and diamond, they lead to non-physical results for the bonding situations intermediate between the single and double bonds, such as the bonding in the Kekule construction for the graphite where, due to bond conjugation, each bond is considered to be approximately one-third double-bond and two-thirds single-bond in character. To correct for this, and similar problems in hydrocarbons, as well as to correct for the non-physical overbinding of radicals, Brenner [40] has developed a Tersoff-type potential for hydrocarbons that can model the bonding in a variety of small hydrocarbon molecules as well as in diamond and graphite. In this potential, equations (8) and (9) are written as

$$H_I^{Br} = \frac{1}{2}\sum_i \sum_{i\neq j} V(r_{ij}) \tag{11}$$

and

$$V(r_{ij}) = f_c(r_{ij})\left[V^R(r_{ij}) + \bar{b}_{ij} V^A(r_{ij})\right], \tag{12}$$

where

$$V^R(r_{ij}) = \frac{D_{ij}}{S_{ij}-1} e^{-\sqrt{2S_{ij}}\,\beta_{ij}(r_{ij}-R_{ij}^{(e)})},$$

$$V^A(r_{ij}) = \frac{-D_{ij}S_{ij}}{S_{ij}-1} e^{-\sqrt{2/S_{ij}}\,\beta_{ij}(r_{ij}-R_{ij}^{(e)})},$$

$$\bar{b}_{ij} = \frac{(b_{ij}+b_{ji})}{2} + F_{ij}\left(N_i^{(t)}, N_j^{(t)}, N_{ij}^{conj}\right),$$

$$b_{ij} = \left[1 + G_{ij} + H_{ij}\left(N_i^{(H)}, N_i^{(C)}\right)\right]^{-\delta_i},$$

$$G_{ij} = \sum_{k\neq i,j} f_c(r_{ik}) G_i(\theta_{ijk}) e^{\alpha_{ijk}\left[\left(r_{ij}-R_{ij}^{(e)}\right)-\left(r_{ik}-R_{ik}^{(e)}\right)\right]},$$

$$G_c(\theta) = \alpha_0\left[1 + \frac{c_0^2}{d_0^2} - \frac{c_0^2}{d_0^2 + (1+\cos\theta)^2}\right]. \tag{13}$$

The quantities $N_i^{(C)}$ and $N_i^{(H)}$ represent the number of C and H atoms bonded to atom i, $N_i^{(t)} = (N_i^{(C)} + N_i^{(H)})$ is the total number of neighbours of atom i and its values, for neighbours of the two carbon atoms involved in a bond, can be used to determine if the bond is part of a conjugated system. For example, if $N_i^{(t)} < 4$, then the carbon atom forms a conjugated bond with its carbon neighbours. N_{ij}^{conj} depends on whether an ij carbon bond is part of a conjugated system. These quantities are given by

$$N_i^{(H)} = \sum_{l\neq i,j}^{\text{hydrogen atoms}} f_c(r_{il}),$$

$$N_i^{(C)} = \sum_{k\neq i,j}^{\text{carbon atoms}} f_c(r_{ik}),$$

$$N_{ij}^{conj} = 1 + \sum_{k\neq i,j}^{\text{carbon atoms}} f_c(r_{ik})\,F(x_{ik}) + \sum_{l\neq i,j}^{\text{carbon atoms}} f_c(r_{jl})\,F(x_{jl}),$$

$$F(x_{ik}) = \begin{cases} 1, & x_{ik} \le 2, \\ \frac{1}{2} + \frac{1}{2}\cos[\pi(x_{ik}-2)] & 2 < x_{ik} < 3, \\ 0, & x_{ik} \ge 3 \end{cases}$$

$$x_{ik} = N_k^{(t)} - f_c(r_{ik}). \qquad (14)$$

The expression for N_{ij}^{conj} yields a continuous value as the bonds break and form, and as second-neighbour coordinations change. For $N_{ij}^{conj} = 1$, the bond between a pair of carbon atoms i and j is not part of a conjugated system, whereas for $N^{conj} \ge 2$ the bond is part of a conjugated system.

The functions H_{ij} and F_{ij} are parameterized by two- and three-dimensional cubic splines respectively, and the potential parameters in eqs. (11) to (14) were determined by first fitting to systems composed of carbon and hydrogen atoms only, and then the parameters were chosen for the mixed hydrocarbon system. Two sets of parameters, consisting of 63 and 64 entries, are listed in [40]. These parameters were obtained by fitting to a variety of hydrocarbon data sets, such as the binding energies and lattice constants of graphite, diamond, simple cubic and fcc structures, and the vacancy formation energies. The complete fitting sets are given in Tables 1-3 in [40].

The above potential was recently further refined [41] by including improved analytic functions for the *intra*molecular interactions, and by an extended fitting data base, resulting in a significantly better description of bond lengths, energies and force constants. In this improved version, the terms in eq. (12) are re-defined as

$$V^R(r_{ij}) = f_c(r_{ij})\left[1 + \frac{Q_{ij}}{r_{ij}}\right]A_{ij}e^{\alpha_{ij}r_{ij}},$$

$$V^A(r_{ij}) = -f_c(r_{ij})\sum_{(n=1,3)} B_{ijn}e^{\beta_{ijn}r_{ij}},$$

$$\bar{b}_{ij} = \frac{\left(p_{ij}^{\sigma\pi} + p_{ji}^{\sigma\pi}\right)}{2} + p_{ij}^{\pi},$$

$$p_{ij}^{\pi} = \pi_{ij}^{rc} + \pi_{ij}^{dh},$$

$$p_{ij}^{\sigma\pi} = \left[1 + G_{ij} + P_{ij}\left(N_i^{(H)}, N_i^{(C)}\right)\right]^{-\frac{1}{2}},$$

$$G_{ij} = \sum_{k\neq i,j} f_c(r_{ik})\,G_i(\cos(\theta_{jik}))e^{\lambda_{ijk}(r_{ij}-r_{ik})},$$

$$\pi_{ij}^{rc} = F_{ij}\left(N_i^{(t)}, N_j^{(t)}, N_{ij}^{conj}\right),$$

$$N_{ij}^{conj} = 1 + \left[\sum_{k\neq i,j}^{\text{carbon atoms}} f_c(r_{ik})\,F(x_{ik})\right]^2 + \left[\sum_{l\neq i,j}^{\text{carbon atoms}} f_c(r_{jl})\,F(x_{jl})\right]^2,$$

$$\pi_{ij}^{hd} = T_{ij}\left(N_i^{(t)}, N_j^{(t)}, N_{ij}^{conj}\right) \left[\sum_{k\neq i,j}\sum_{l\neq i,j}(1-\cos^2\omega_{ijkl})\,f_c(r_{ik})\,f_c(r_{jl})\right],$$

$$\cos\omega_{ijkl} = e_{ijk}.e_{ijl} \qquad (15)$$

Q_{ij} is the screened Coulomb potential, which goes to infinity as the inter-atomic distances approach zero. The term π_{ij}^{rc} represents the influence of radical energetics and π-bond conjugation on the bond energies, and its value depends on whether a bond between atoms i and j has a radical character and is part of a conjugated system. The value of π_{ij}^{dh} depends on the dihedral angle for the C-C double bonds. P_{ij} represents a bicubic spline, F_{ij} and T_{ij} are tricubic spline functions. In the dihedral term, π_{ij}^{dh}, the functions e_{jik} and e_{ijl} are unit vectors in the direction of the cross products $\mathbf{R}_{ji}\times\mathbf{R}_{ik}$ and $\mathbf{R}_{ij}\times\mathbf{R}_{jl}$ respectively, where the **R**'s are the inter-atomic vectors. The function $G_c(\cos(\theta_{jik}))$ modulates the contribution that each nearest-neighbour makes to $\bar{b}_{ij}$. This function was determined in the following way. It was computed for the selected values of θ=109.47° and θ=120°,

corresponding to the bond angles in diamond and graphitic sheets, and for θ=90° and θ=180°, corresponding to the bond angles among the nearest neighbours in a simple cube lattice. The fcc lattice contains angles of 60°, 90°, 120° and 180°. A value of $G_c(\cos(\theta=60°))$ was also computed from the above values. To complete an analytic function for the $G_c(\cos(\theta))$, sixth order polynomial splines in $\cos(\theta)$ were used to obtain its values for θ between 109.47° and 120°. For θ between 0° and 109°, for a carbon atom i, the angular function

$$g_c = G_c\left(\cos(\theta)\right) + Q(N_i^t).\left[\gamma_c\left(\cos(\theta)\right) - G_c\left(\cos(\theta)\right)\right], \tag{16}$$

is employed, where $\gamma_c(\cos(\theta))$ is a second spline function, determined for angles less than 109.47°. The function $Q(N_i^t)$ is defined by

$$Q(N_i^t) = \begin{cases} 1, & N_i^t \le 3.2, \\ \frac{1}{2} + \frac{1}{2}\cos\frac{\pi(N_i^t - 3.2)}{(3.7-3.2)}, & 3.2 < N_i^t < 3.7, \\ 0, & N_i^t \ge 3.7 \end{cases} \tag{17}$$

The large data base of the numerical data on parameters and spline functions for this potential are available from [42]. These parameters were obtained by fitting the elastic constants, vacancy formation energies and the formation energies for interstitial defects for diamond.

3.2 The C-C non-bonding potentials

The non-bonding interactions between carbon atoms are required in some of the simulation studies reported in this review. These can be modelled according to various types of potentials. We have employed the Lennard-Jones potential to describe the van der Waals inter-molecular interactions between such systems as C_{60} molecules, and between the basal planes in a graphite lattice. Other useful potentials are the 6-exp potential [43] which also describes the C_{60}-C_{60} interactions, and the Ruoff-Hickman potential [44] which models the C_{60}-graphite interactions.

3.2.1 The Lennard-Jones potential

The total interaction potential between the carbon atoms in two C_{60} molecules, or between those in two graphite basal planes, can be represented by the Lennard-Jones potential [45]

$$H_I^{LJ}(r_{ij}^{IJ}) = 4\varepsilon \sum_i \sum_{j>i} \left[\left(\frac{\sigma}{r_{ij}^{IJ}}\right)^{12} - \left(\frac{\sigma}{r_{ij}^{IJ}}\right)^{6} \right], \tag{18}$$

where I and J denote the two molecules (planes), r_{ij}^{IJ} is the distance between the atom i in molecule (plane) I and atom j in molecule (plane) J. The parameters of this potential, ($\varepsilon=0.24127\times10^{-2}$ ev, $\sigma=3.4\,\mathring{A}$), were taken from a study of graphite [46].

3.2.2 The 6-exp potential

This is another potential that describes the interaction between the carbon atoms in two C_{60} molecules

$$H_I^{DJ}(r_{ij}^{IJ}) = \sum_i \sum_{j>i} -\frac{A}{(r_{ij}^{IJ})^6} + Be^{-\alpha r_{ij}^{IJ}}. \tag{19}$$

Two sets of values of the parameters are provided, and these are listed in Table 2. These parameters have been obtained from the gas phase data of a large number of organic compounds, without any adjustment. The measured value of the C_{60} solid lattice constant is $a=14.04\,\mathring{A}$ at T=11 K. The calculated value using the set one was $a=13.01\,\mathring{A}$ and using the set two was $a=14.03\,\mathring{A}$. The experimentally estimated heat of sublimation is equal to -45 kcal/mol (extrapolated from the measured value of -40.1±1.3 kcal/mol at T=707 K). The computed value using the set one was -41.5 kcal/mol and using the set two was -58.7 kcal/mol. We see that whereas the set two produces a lattice constant nearer the experimental value, the thermal properties are better described by using the set one.

Table 2. Parameters of the 6-exp potential for C.

	A (kcal/mol× $\mathring{A}^6$)	B (kcal/mol)	α $\mathring{A}^{-1}$
set one	358	42000	3.58
set two	568	83630	3.60

3.2.3 The Ruoff-Hickman C_{60}-graphite potential

This potential, based on the model adopted by Girifalco [47], describes the interaction of a C_{60} molecule with a graphite substrate by approximating these two systems as *continuum* surfaces on which the carbon atoms are 'smeared out' with a uniform density. The sums over the

pair interactions are then replaced by integrals that can be evaluated analytically. The C_{60} is modelled as a hollow sphere having a radius $b=3.55\ \mathring{A}$, and the C-C pair interaction takes on a Lennard-Jones form

$$H_I(r_{ij}) = c_{12} r^{-12} - c_6 r^{-6}, \qquad (20)$$

with c_6=19.97 eV $\mathring{A}^6$ and c_{12}=34812 eV $\mathring{A}^{12}$ [47]. The interaction potential between the hollow C_{60} and a single carbon atom of a graphite substrate, located at a distance z>b from the centre of the sphere, is then evaluated as

$$H^{RH}(z) = H_{12}(z) - H_6(z), \qquad (21)$$

where

$$H_n(z) = \frac{c_n}{2(n-2)} \frac{N}{bz} \left[\frac{1}{(z-b)^{n-2}} - \frac{1}{(z+b)^{n-2}} \right], \qquad (22)$$

where N is the number of atoms on the sphere (N=60 in this case) and n=12,6. The total interaction energy between the C_{60} and the graphite plane is then obtained by integrating $H^{RH}(z)$ over all the atoms in the plane, giving

$$H_I^{RH}(R) = E_{12}(R) - E_6(R), \qquad (23)$$

where

$$E_n(R) = \frac{c_n}{4(n-2)(n-3)} \frac{N^2}{b^3} \left[\frac{1}{(R-b)^{n-3}} - \frac{1}{(R+b)^{n-3}} \right], \qquad (24)$$

and R is the vertical distance of the cetre of the sphere from the plane.

4. Formation of nano-scale films on supporting substrates

Atomistic modelling of the formation of low-dimensional semi-conducting films on supporting substrates has formed an active area of research. This process is a highly complex vapour-to-solid heterogeneous phase transition phenomenon in which an initial condensation of the impinging atoms, or clusters, is followed by their surface diffusion, coalescence and the eventual growth into layered structures. Three nucleation and growth modes have been distinguished [48]. These are the Volmer-Weber, the Frank-van der Merwe and the Stranski-Krastanov modes. In the Volmer-Weber mode, small clusters are first nucleated *directly* on the substrate surface. These then diffuse on the surface, coalesce and grow into islands. This happens when the adatoms, or clusters, interact far more strongly among themselves than with the underlying substrate. This mode is displayed by many systems of metals growing on insulators, including many metals grown on alkali halides, graphite and other compounds such as mica. The Frank-van der Merwe mode is realised when the adatoms interact far more strongly with the substrate than with each other. In this mode, the first atoms to condense on the surface form a *complete* monolayer directly. This is then followed by the formation of the next layer which is much less tightly bound to the first layer. This mode is observed in the growth of rare gases on graphite and on several metals, in some metal-on-metal systems, as well as in semi-conductor growth on semi-conductors. The Stranski-Krastanov mode occupies an intermediate stage in which there is a *mixed* mode of layer-plus-island growth. In this mode, following the formation of the first few layers, the layer growth becomes unfavourable and islands are formed on the top of the layers. This mode is realised in the metal-on-metal, metal-on-semiconductor and gas-on-metal systems.

In all these modes, single atoms, or clusters, arriving at the substrate from a gas phase, or a cluster-beam phase, are in highly exited states and are not initially in thermal equilibrium with the supporting substrate. They then undergo several types of individual and collective motions on the surface before they eventually condense on the surface; they may migrate over the surface by hopping from one well in the substrate's potential to another due to their thermal activation and/or their own kinetic energy parallel to the surface, or they may desorb and escape back into the gas phase, or nucleate two- and three-dimensional local clusters during finite residence time on the surface by interacting with other adatoms, or implant into the substrate, or be captured at special defect sites such as kinks and dislocations. The initial condensation is therefore a competition between these events, i.e. the adsorption and desorption equilibrium processes. The determining factor is the interaction at the interface which controls the growth mode.

One area of recent and active research concerning the formation of thin films has been the *controlled* nucleation and growth of nano-scale films composed of *clusters*. Detailed knowledge of cluster-substrate interactions and cluster diffusion on substrates is essential in many technological applications ranging

from sputtering to the formation of defect-free films that will play a fundamental role in the next phase of the *miniaturisation programme*, which forms an important component of the top-down approach to nano-technology, and whose aim is the design and fabrication of quantum-scale devices. An important aspect of this cluster-on-substrate research has been the controlled adsorption of C_{60} molecules on technologically important metallic and semi-conducting substrates. The information obtained on the growth mode and morphology of the first few layers will help determine the properties of the resulting C_{60} films.

In Section 5, we consider two examples of application of MD simulation to the problem of nanoscopic nucleation and growth of semi-conducting films on supporting substrates. These simulations investigate the adsorption of C_{60} molecules on the Si(100) and graphite (0001) surfaces In both cases the relevant experiments are first summarized in Section 4.1.

4.1 A review of the experimental results on adsorption of C_{60} molecules on metallic and semi-conducting surfaces

The C_{60} fullerene molecule, shown in Fig.1, was discovered in 1985 [49]. It consists of 60 carbon atoms, located on 12 pentagons and 20 hexagons. It forms the third allotrope of the stable state of condensed carbon, along side graphite and diamond. The molecule has a high symmetry, with 120 symmetry operations that map it onto itself. Its synthesization in macroscopic amounts [50] led to the emergence of the new field of *fullerene-based physics and chemistry*.

Fig. 1. The structure of C_{60} molecule, showing the pentagons and the hexagons

Some of the basic properties of C_{60} molecule are:

Average C-C distance	1.44 Å
Mean diameter	6.83 Å
Outer diameter	10.18 Å
Inner diameter	3.48 Å
Mass density	1.72 g/cm^3
Molecular density	1.44×10^{21}/cm^3
Bulk modulus	14 Gpa
Structural phase transitions	255 K, 90 K
Binding energy per atom	7.4 eV

Following C_{60}, a whole family of fullerenes including C_{70}, C_{76}, C_{84}, C_{90}, C_{96} and the much larger quasi-spherical fullerenes, C_{888}, C_{1020} ,C_{1500} [51], have been identified.

Early experimental study [52] and computation [53] of C_{60} properties predicted its truncated icosahedral soccer-ball hollow-cage geometry having an usual degree of stability. Band structure calculations [53], based on the density functional formalism, showed that C_{60} molecules form a weakly bound van der Waals fcc *semi-conducting* crystal (lattice constant=14.17 Å) with a band gap of 1.7 eV between the *highest occupied molecular orbital* (HOMO) and the *lowest unoccupied molecular orbital* (LUMO) levels. In this crystal, the centre-to-centre separations of the molecules are 10.02 Å , the C_{60}-C_{60} cohesive energy is 1.6 eV, the melting temperature is 1180°C, the sublimation temperature is 434°C, the heat of sublimation is 40.1 kcal/mol and the latent heat is 1.65 eV/C_{60} [54]. Furthermore, the molecules undergo 10^9 free rotations per second under the ambient conditions [55]. Another interesting property of C_{60} is its doped state, whereby the introduction of alkali metal atoms into the molecule produces superconducting compounds with a transition temperature in excess of T=30 K [56].

In the following subsections we review the main results on the adsorption of C_{60} molecules on a set of metallic, semi-metallic and semi-conducting substrates. These substrates are: Au(110), Ag(110), Ni(110),

Cu(111), Ag(111), Au(111), graphite (HOPG), Si(100), Si(111).

4.1.1 Adsorption of C_{60} on Au, Ag, Ni and Cu substrates

Early STM-based investigations on the adsorption of C_{60} molecules on the Au(111) surface [57, 58] showed that the adsorbed layer consisted of a close-packed unstable structure composed of mobile hexagonal arrays of sub-clusters with a spacing of 11 $\mathring{A}$. The Au(111) surface is a $c(2\sqrt{3}\times 2\sqrt{3})$ reconstructed surface whose lattice parameter is fairly close to the nearest-neighbour distance in the bulk fcc C_{60} crystal. Further studies of the adsorption of C_{60} molecules on this surface [59, 60] showed that two morphologies could be identified in the absorbed layer; an alignment commensurate with the $c(2\sqrt{3}\times 2\sqrt{3})$ reconstruction, and another having a c(38×38) structure, indicating a growth from the <110> step edge.

Another interesting Au surface is the Au(100) which has a c(5×20) reconstruction along the <110> direction. The adsorption on this surface [61] showed that the existing dislocations and ridges in the reconstruction formed preferential nucleation sites. It was also observed that there was a dilation of the nearest-neighbour distance between the adsorbed molecules as compared with the distance in the bulk C_{60}, indicative of the presence of stress in the monolayer along the <110> direction.

The Ag(111) surface has a reconstruction similar to the Au(111) surface. Its $c\left(2\sqrt{3}\times 2\sqrt{3}\right)$ reconstruction is rotated by 30°. The adsorption on this surface [60, 62] showed a commensurate first layer, with some alignments in parts of the layer rotated by 10° and 15°.

The adsorption on the Au(110) and the Ag(110) surfaces were investigated in STM-based experiments [63, 64], and it was found that the adsorption *induced* a modification of the existing reconstruction on the Au surface when the system was annealed at T=700 K. This surface modification resulted in the formation of a close-packed C_{60} monolayer with a c(6×5) periodicity relative to an unreconstructed Au surface. No induced reconstruction was, however, observed on the unreconstructed Ag surface.

The STM-based investigation on the adsorption on the Cu(111)c(1×1) surface [65] showed that the molecules in the first layer were mobile on the terrace and were stabilized at the step edges, and with the increase in coverage a well-ordered two-dimensional island with a c(4×4) triangular symmetry began to form on the first layer.

The question of *charge transfer* (CT) to C_{60} molecules adsorbed on metallic surfaces was addressed in a *low-energy-electron-diffraction* (LEED) experiment [66] where the Au(110), the polycrystalline Ag(110) and the Ni(110) surfaces were employed as substrates. The aim was to compare the transfer from the rather inert noble metal surfaces with the transfer from a transition metal surface. The experiment provided quantitative estimates of this CT, which was found to be (1±1) electrons from the Au(110) and Ag(110) surfaces and (2±1) electrons from the Ni(110) surface. These values demonstrated that the CT was strongly dependent on the type of metal rather than its work function, since the work function of the Ni(110), at 5.04 eV, is in between that of the Au(110), at 5.37 eV, and the polycrystalline Ag, at around 4.6 eV. These results supported the proposal [67] that the CT is due to the formation of chemical bonds between the adsorbed C_{60} molecules and the metallic surfaces. The magnitudes of the CT were estimated from the softening of the vibrational frequencies of the C_{60} molecules upon their adsorptions on the surfaces.

The alignments adopted by the adsorbed molecules were also determined in this LEED experiment and it was found that in the low-coverage regime the adsorbed overlayer structure on the Ni(110) surface differed significantly from those observed on the Au and Ag surfaces. The stronger C_{60}-Ni interactions, due to a larger amount of CT, had led to the formation of a novel rectangular Ni(110)-c(5×3) C_{60} morphology, as compared with the close-packed islands observed on the noble metal surfaces, which were nucleated on the substrates' terraces.

The charge distribution on C_{60} molecules has also been determined for the adsorption on the Cu(111)c(1×1) surface [68]. The STM images [65] of this distribution showed a strong bias-voltage dependence. The image of the empty electronic states of an absorbed C_{60} showed a *three-leaf clover* shape for each adsorbed molecule, indicative of a rotationally well-ordered state of the molecules. The computed two-dimensional (2D) band structure and partial charge-density distribution [69] for

the c(4×4) 2D structure, mentioned before, showed that three different distributions can be associated with the energy levels; a round shape with a hole in the middle in the HOMO-like states, a round shape without a hole, and a three-fold symmetry representing the three pentagonal C rings in the LUMO-like states. These distributions were very similar to those observed in the STM images at *different* bias voltages [65].

4.1.2 Adsorption of C_{60} on Si and graphite substrates

The reconstructed Si surfaces, Si(111)c(7×7) and Si(100)c(2×1), play a very important role in the electronic device fabrication, and will play an even more significant role in the anticipated nano-technology. They have, therefore, provided very interesting substrates for the growth of monolayers and multilayers of adsorbates, such as the epitaxial growth of C_{60} films. In contrast to the inert metallic surfaces, such as Au, the Si(100) dimerized surface [70] is a very *active* surface where each Si atom contributes a *dangling* bond. It is therefore expected that a considerable amount of CT would be involved when a C_{60} molecule is adsorbed on this surface. Such a strong coupling between a C_{60} molecule and the Si(100) surface would be expected to lead to a cessation of its rotational diffusion upon adsorption. For the Si(111) surface, on the other hand, each corner hole atom, adatom and rest atom has a dangling bond [68].

The STM investigation on the adsorption of C_{60} on the Si(111)c(7×7) surface [71] showed that due to the much stronger adsorbate-substrate interactions, the C_{60} molecules were randomly adsorbed on the surface. Another STM-based experiment [72] revealed the adsorption sites within the c(7×7) surface unit cell, where the molecules favoured adsorption on the faulted half of the unit cell as compared with the unfaulted half, since the former is more energetic with a larger density of states near the Fermi level. Occasionally molecules were adsorbed on the corner vacancies, but very little adsorption on the dimer lines was observed.

The adsorption on the Si(100)c(2×1) surface was reported in a field-ion STM (FI-STM) experiment [73, 74, 75]. Since this experiment forms the basis of one of the numerical simulation studies that we have carried out, and which will be reported in Section 5, we here summarize its main conclusions, arrived at on the basis of a large number of STM images, concerning the final alignments of the adsorbed molecules:

1. The adsorbed molecules resided in the valleys of the dimer rows on the Si surface and were distributed randomly with a minimum inter-molecular separation of 12 Å when the C_{60} density was small.
2. The individual molecules occupied site A, schematically shown in Fig.2, with a high degree of symmetry and were surrounded by 8 dimer-forming Si atoms.
3. Unlike the adsorption on the GaAs(110) surface [76], no coalescence on the terraces and segregation to the steps or defect sites were observed.
4. There was a short-range local ordering of the molecules in the first layer. Two types of structures could be distiguished; a c(4×4) alignment and a c(4×3) alignment, as can be seen in the STM image shown in Fig.3 . The c(4×3) forms the fcc(111) plane as well as the hcp basal plane, and the c(4×4) forms the (001) plane of a simple cube. The nearest-neighbour distances were 9.6 Å and 10.9 Å for the c(4×3) and c(4×4) respectively.
5. With the completion of the first layer, the second layer began to form. Island formation was also observed, signalling a Stranski-Krastanov mode of growth.
6. STM images were obtained that showed structures on individual adsorbed molecules. The STM image in Fig.4 shows three or four bright *stripes* running in parallel on each molecule. Since the orientations of these stripes were the same, this was taken to indicate that the rotating molecules had ceased their rotations once they had been absorbed on the surface. The origin of these stripes was attributed to the CT from the dimerized surface.

Investigation of the adsorption of C_{60} molecules on a graphite surface forms an interesting topic due to a strong similarity in the electronic and geometrical structures of these two materials. Several experimental investigations on this system have been reported over the recent years. The structural and vibrational properties of the C_{60} film adsorbed on the surface of highly oriented pyrolytic graphite (HOPG) were examined in a *high resolution electron energy loss spectroscopy* (HREELS) experiment [77]. A novel high-order periodicity at monolayer coverages was observed, implying that even the weak corrugation potential of the surface was sufficient to perturb the adlayer, and that the C_{60}s were

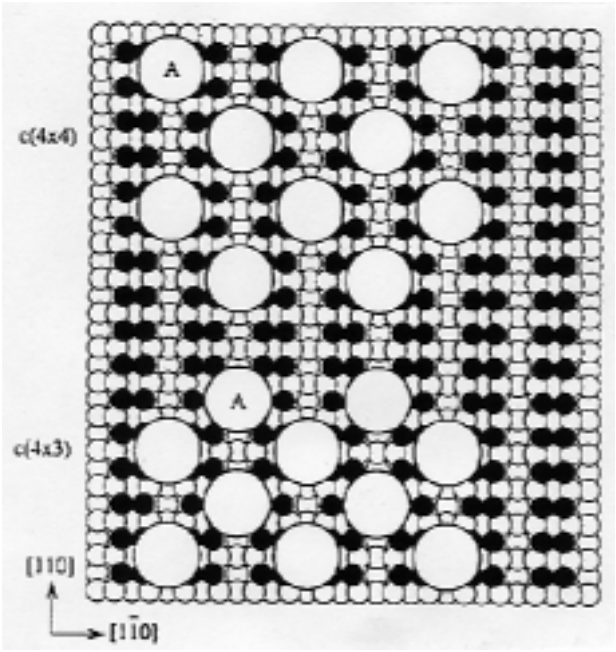

Fig. 2. Schematic positions of C_{60} molecules that form c(4×3) and c(4×4) lattices on Si(100) c(2×1) surface. Open circles are Si atoms bulk positions, solid circles are dimerized Si atoms and large open circles indicate position of C_{60} molecules. Figure from [73].

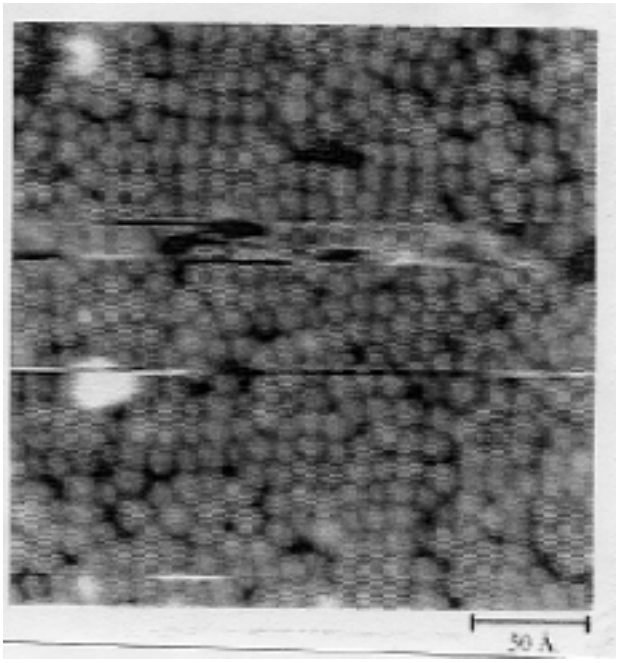

Fig. 3. STM image of the Si(100) surface with approximately one monolayer coverage of C_{60} molecules showing both the c(4×3) and c(4×4) packings. The regions are still unfilled bare Si surface. Fig. taken from [73].

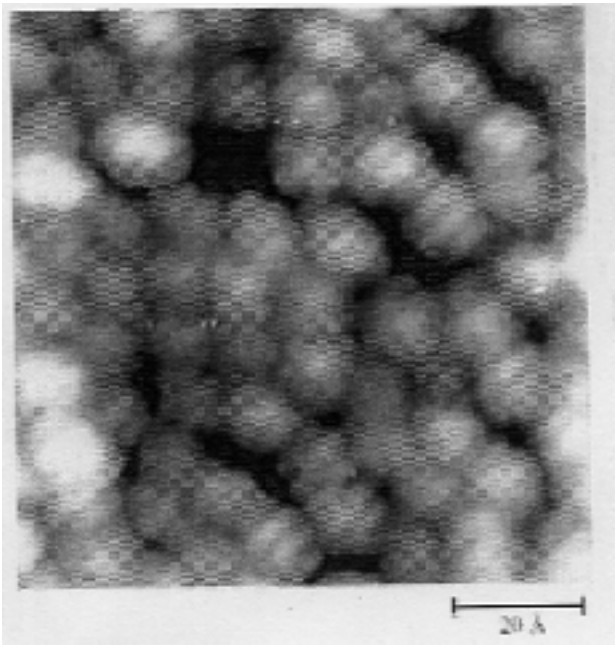

Fig. 4. STM image of the first layer of the C_{60} molecules on the Si(100) surface. The image shows some internal structure in the form of bright stripes running in parallel on the molecules. Fig. taken from [73].

physisorbed on the graphite. Another HREELS-based experiment [78] on the early stages in growth at room temperature suggested a predominantly layer-by-layer growth of two-dimensional islands, while a combined HREELS-and-STM-based experiment [79, 80] showed that the adsorbed molecules aggregated to form asymmetric *dendrite-like* islands, as shown in Fig.5a, implying a high mobility on the surface. Higher magnification of the STM images in this experiment also revealed that the C_{60}s arranged themselves in a hexagonal close-packed morphology, as shown in Fig.5b, and two crystallographic directions were identified. The growth mode on the surface was found to be consistent with both the Frank-van der Merwe layer-by-layer mode and the mixed monolayer-plus-island Stranski-Krastanov mode.

Very recently, another STM-based experiment [81], performed at substrate temperatures of T= 300 K and T=373 K, has examined the influence of the deposition rate and the temperature, and the influence of naturally occurring surface steps on the growth of C_{60} islands. At room temperature, multilayer islands of C_{60}, of different sizes, were nucleated predominately at the step edges, as shown in Fig. 6, with a negligible formation on the terraces. Unlike in other studies, a simple layer-by-layer

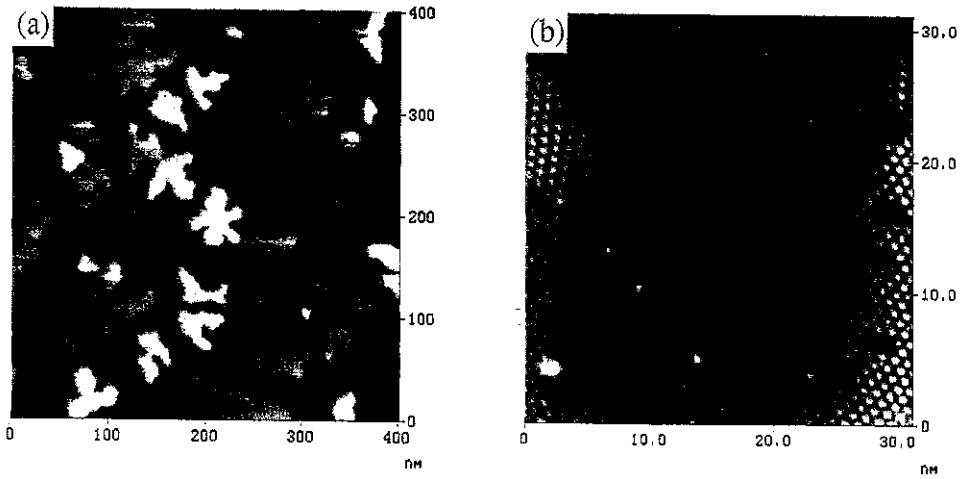

Fig. 5. STM images of C_{60} film on the graphite surface at coverage of 1.8 ML: (a) The size of the image is 400×400 nm; the sample bias is 2.4 V; the tunnelling current is 290 pA. (b) The size of the image is 30×30 nm; the sample bias is 2.1 V; the tunnelling current is 190 pA. Figure taken from [80].

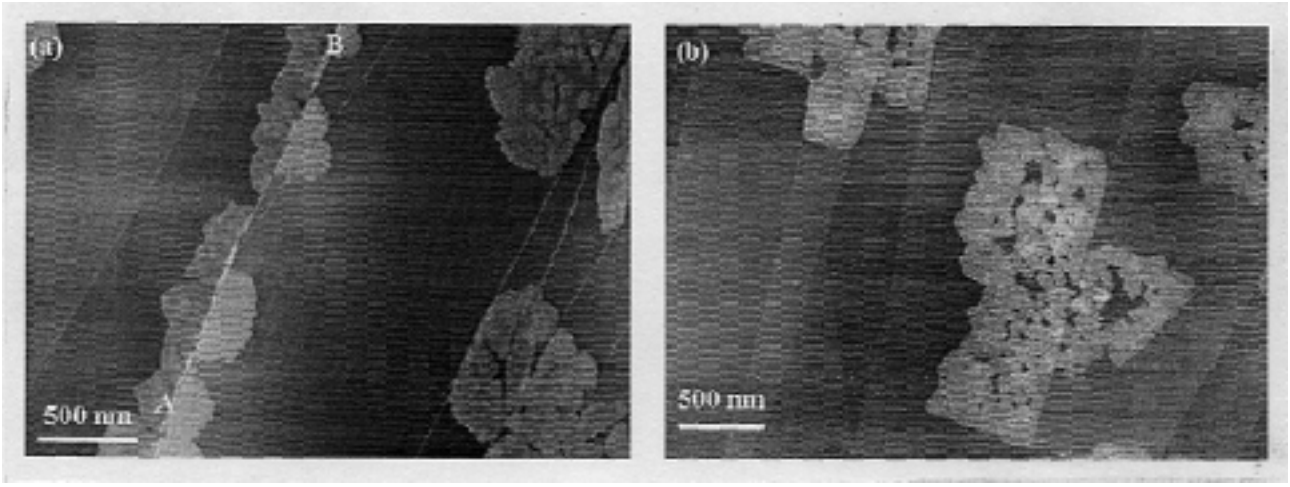

Fig. 6. (a) 2.2 mm×3.0 mm scan of 1 ML C_{60} coverage on HOPG deposited at a rate of 0.07 ML min^{-1}. (b) 2.5 mm×3.5 mm scan of 1 ML C_{60} deposited at a slower rate of 0.035 ML min^{-1}. The step height of the islands is 18.8 Å averaged over several readings. Figure taken from [81].

growth mode was only observed at the elevated temperature. The origin of a 3D growth was found to be an initial bilayer, rather than a monolayer, formation. Islands with faceted edges were nucleated when the deposition rate was lowered, indicating that the molecules arriving at an island edge had now sufficient time to diffuse around the island and take up a more ordered equilibrium position.

In addition to these STM-based experiments conducted under *ultra-high vacuum* (UHV) conditions, the results of another STM-based experiment, performed in air [82], where the C_{60} molecules were adsorbed from a solution onto HOPG, have also been reported. The results showed that the molecules formed clusters of various sizes that tended to aggregate further. Detailed examination of the STM images revealed what were claimed to be extra `real' features, in the form of *ridges* and *bumps*, on individual molecules. The origins of these features could not, however, be unambiguously identified and they were attributed to electronic states *induced* either by the action of the HOPG substrate or by the STM tip on the charge states of the C_{60} molecules.

5. Constant temperature MD simulations

In this Section, we report on our results of two highly

complex MD simulations to model the *dynamic* process of adsorption of C_{60} molecules on the Si(100)c(2×1) surface [83, 84] and on a graphite substrate [85]. The pertinent experiments underlying these simulations, [73] for Si(100), and [80, 82] for the graphite, were discussed in Section 4. The MD simulations that are reported here were of equilibrium type applied to canonical ensembles.

5.1 C_{60}/Si(100) system

For the simulation of this complex system, we treated the C_{60}s as both flexible and rigid molecules. Three inter-atomic potentials were employed to describe the interactions between the Si-Si atoms in the substrate, the C-C atoms in different molecules and the C-Si atoms at the interface:

1. The Si-Si and C-Si interactions are covalently-bonding, and were described by the unified many-body Tersoff potentials given in eq. (8).
2. The non-bonding C-C interactions between the atoms in two molecules were described by the Lennard-Jones potential given in eq. (18).

The Si substrate consisted of 9 atomic layers with 128 atoms per layer. With the exception of the lowermost Si atoms, all the other substrate atoms were treated dynamically. Periodic boundary conditions were applied in all three spatial directions. In the initial state, shown in Fig.7a, 14 molecules were randomly distributed above the <100> dimerized surface. The system was equilibrated for 1000 time steps ($dt=10^{-14}$ s) at the constant temperature of T=300 K and constant pressure by treating the volume of the simulation cell as a variable. The temperature was maintained at this value during this phase, and indeed throughout the simulation, by implementing the Nose'- Hoover thermostat, whose equations of motion are given in eq. (6). During this equilibration phase, no interactions were allowed between the molecules and the surface. Fig. 7b shows the configuration of the system after equilibration. Following equilibration, the volume of the computational cell was fixed at its relaxed value, and the molecules were simultaneously released in the direction of the substrate. The animation of the complete run, using three-dimensional visualisations, showed that the molecules performed continuous bouncing interactions, with each other and with the surface, before they were adsorbed on, and equilibrated with the surface. Fig. 7c shows the final state, where the molecules came to rest in the dimer valleys of the surface and were surrounded by eight dimer-forming Si atoms, exactly as was predicted in the FI-STM experiment [73] discussed above. Furthermore, Fig. 7d shows the presence of a c(4×4) alignment where, for convenience, we have not shown those molecules undergoing PBC. This result was also in agreement with the experimental finding [73].

In a further, larger, simulation [84] we increased the size of the system. The substrate still consisted of 9 layers, but with 512 atoms per layer, and the initial state was now composed of 220 molecules as opposed to 14. Furthermore, the C_{60}s were treated as flexible molecules, with the intra-molecular interactions described by a simple harmonic potential, and they were *individually* released towards the substrate. The final state of the simulation is shown in Fig.8. As before, the molecules came to rest in the dimer valleys on the surface. However, in this case, both the c(4×4) and c(4×3) alignments were obtained, in complete agreement with the experimental results [73] schematically shown in Fig. 1.

To elucidate the origin of the stripes observed on the molecules in the experiment [73], and shown in Fig.4, we also performed an ab initio band-structure calculation [83] using the mixed-basis all electron Car-Parrinello method [86]. Our results showed that the charge transfer from the substrate was responsible for the emergence of the observed structures.

5.2 C_{60}/graphite(0001) system

In this simulation, the C_{60}s were treated as flexible molecules. Four inter-atomic potentials were used:

1. The non-bonding C-C interactions between the atoms in two graphite basal planes were described by the Lennard-Jones potential given in eq. (18), and between the atoms in two molecules by the 6-exp potential given in eq. (19).
2. The non-bonding C_{60}-graphite interactions at the interface were described by the Ruoff-Hickman potential given in eq. (21). In our adaptation of this potential, only the C_{60}s were modelled as continuum hollow spheres (radius $b=3.55\,\mathring{A}$) during the interfacial interactions, and the graphite substrate was treated as a lattice of individual atoms. Under this approximation, the original form of the Ruoff-Hickman potential, now describing the interaction of a hollow sphere with a single atom of the graphite substrate, took on the form given in eq. (21).

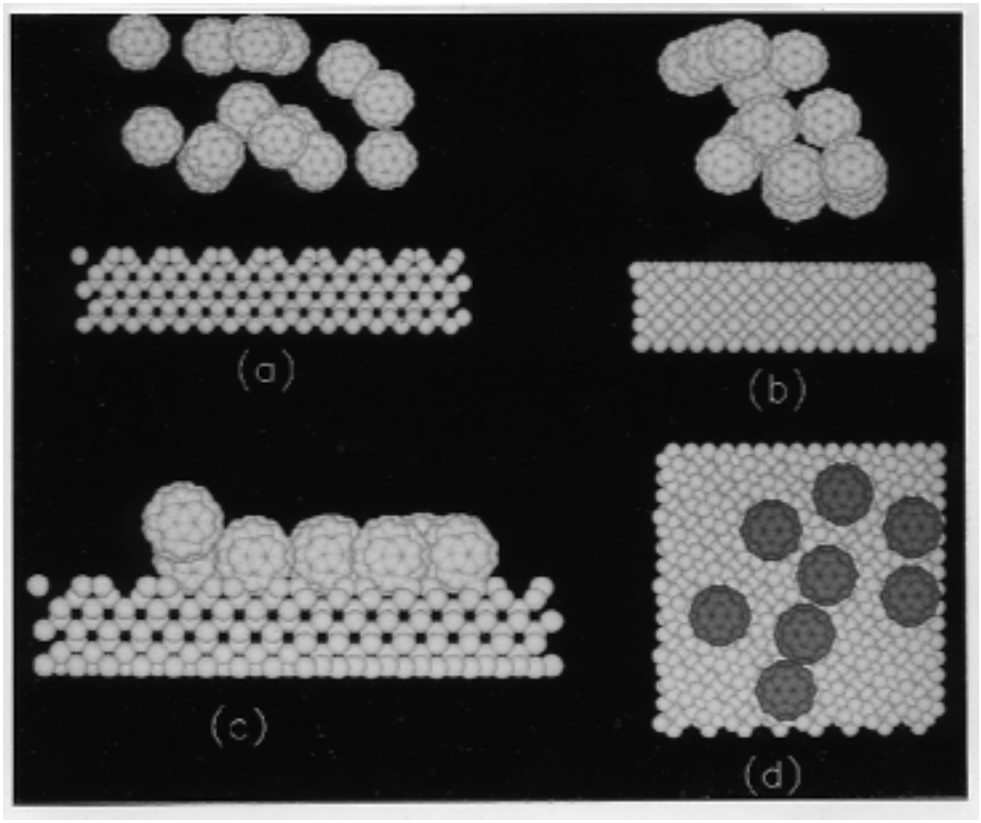

Fig. 7. Three-dimensional (3D) geometries of simulated C_{60}/Si(100) system: (a) initial state with randomly distributed molecules above surface, vertical direction is <001>, horizontal direction is <111> and <110> direction is perpendicular to plane of paper away from reader; (b) after equilibration, horizontal and vertical directions are <100> and <001>; (c) final state with molecules residing in troughs of dimer rows, directions are same as in (a); (d) top view showing alignment of molecules and formation of a c(4×4) packing, horizontal and vertical directions are <100> and <010>.

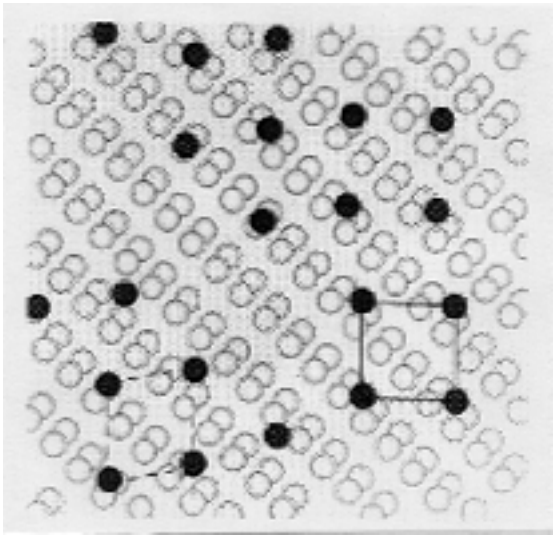

Fig 8. Top view showing alignment of simulated C_{60} molecules on Si(100) surface when 40% of surface was covered. Example of c(4×4) packing (solid lines) and c(4×3) packing (broken lines) is marked in figure. Only centres of mass of molecules (darker circles) are shown.

3. The covalently-bonding C-C intra-molecular and intra-planar interactions were described by the powerful and *improved* many-body Tersoff-type Brenner potentials given in eqs. (11) , (12), (15).

In our MD simulation [85], the initial state, shown in Fig.9a, consisted of 14 *flexible* C_{60} molecules randomly distributed above the top (0001) basal plane of a graphite substrate. The substrate was composed of three planes with, respectively, 448, 448 and 568 atoms in the upper, middle and lower planes. Both terraces and steps were therefore available in the case of terrace diffusion and segregation to the steps. The simulation time step and temperature were set respectively at $dt=10^{-16}$s and T=300 K, and the velocity Verlet algorithm was used to integrate the equations of motion. The simulation temperature was controlled via a Nose'-Hoover thermostat, eq. (6).

The system was equilibrated for 10,000 time steps during which the C_{60}s were not allowed to move in the z-

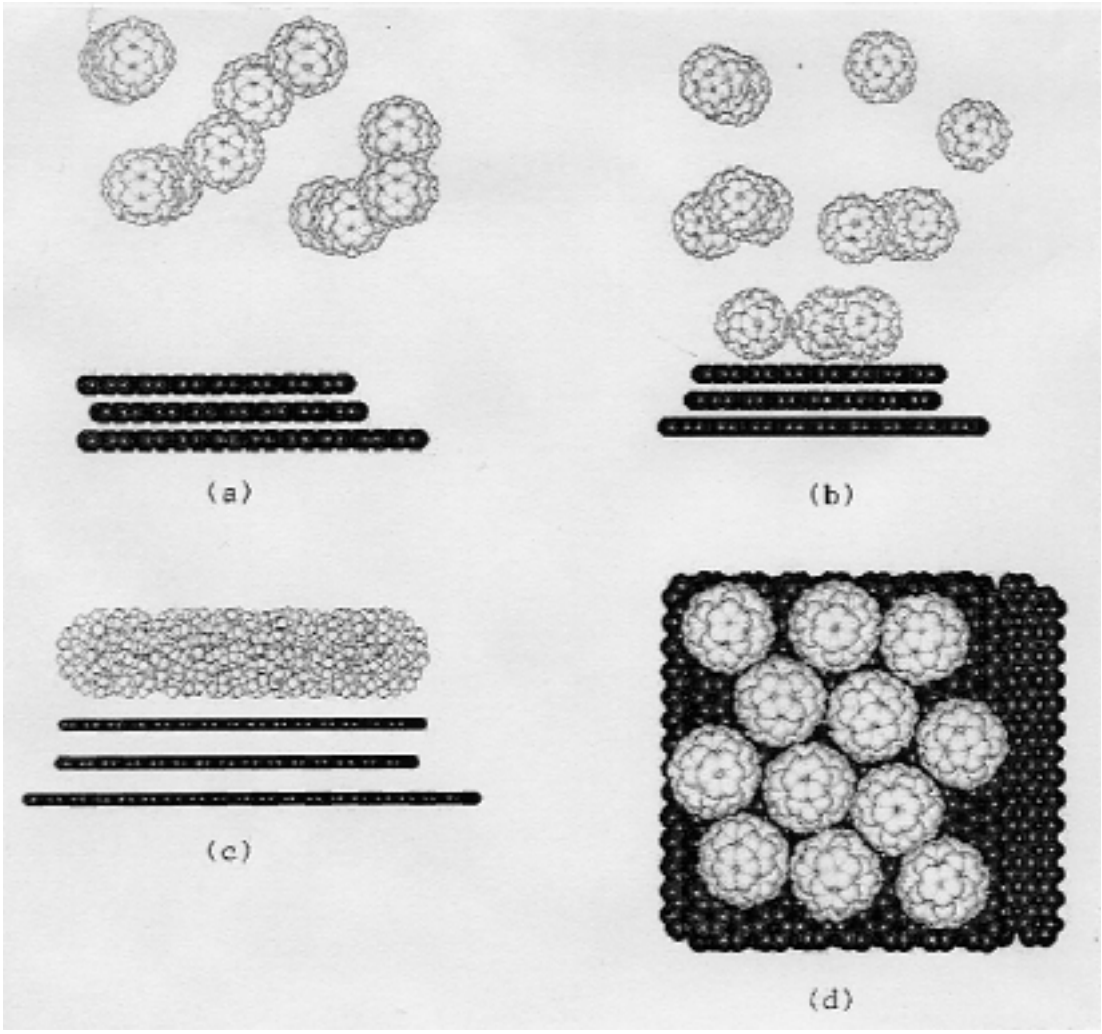

Fig. 9. Three-dimensional (3D) snapshots from MD simulation showing C_{60}-graphite system in: initial state (a); after 22 picoseconds (b); after 161 picoseconds (c); top view after 161 picoseconds (d). The <100> direction runs from left to right.

direction, or interact with each other, or with the substrate. All other interactions, i.e., the intra-molecular, intra-planar and inter-planar interactions were, however, switched on. We observed a small shift of the graphite basal planes relative to their initial states, as shown in Fig.9b.

Following equilibration, the molecules were released towards the substrate, *one at a time*, ensuring that there were no correlations between the molecules prior to their soft-landing and adsorption on the graphite surface. This was a complex *dynamical* adsorption method consisting of the following steps. First a molecule was released from its equilibrated position and its trajectory was followed until it soft-landed on the substrate and equilibrated with it, which happened after it executed several bounce-on bounce-off vertical motions, as well as lateral diffusive motions, over the surface. Upon the adsorption of the molecule, the next one was then released. The states of the molecules already adsorbed on the surface were monitored simultaneously with that of a newly released molecule, i.e. when a new molecule was heading towards the substrate the interactions among those molecules already adsorbed, and between them and the substrate, were also considered at the same time. The C_{60}-C_{60} interactions were switched on only for those molecules that were residing on the surface. If a molecule bounced off the surface, its interactions with the rest of the molecules on the surface were switched off, if the vertical distance of its centre of mass from the substrate exceeded 7 $\mathring{A}$, and were then switched back on if it dropped below this value. Fig.9b shows the snapshot of the system after 3 molecules had soft-landed on the

surface, and Fig.9c shows the final state when 12 out of the 14 molecules had been adsorbed and equilibrated with the substrate; the other 2 molecules, undergoing PBC, are not shown here. Fig.9d shows the top view of Fig.9c. The equilibrium configuration of the 12 adsorbed molecules on the surface was reached after a significant period of 153 picoseconds from the start of the deposition process. The system was re-equilibrated for a further 8 picoseconds during which the molecules showed some surface diffusion before reaching the final alignment shown in Fig.9c, which corresponds to the configuration obtained after 161 picoseconds, i.e., after 1.6 million time steps. The gaps between the centres of mass of the adsorbed molecules and the top basal plane, shown in Fig.9c, vary from 6.47 Å to 6.57 Å. This range is very close to the value 6.52 Å computed by Rey *et al* [87] who employed the Ruoff-Hickman potential to obtain the most stable configurations of C_{60} molecules *supported* by a graphite substrate, i.e., not dynamically deposited during an adsorption process. Our range of values also agrees with the value obtained by Gravil *et al* [88]. In Fig.9d, the centre-to-centre inter-molecular separations are on average 9.9 Å. The alignment of the molecules in this figure strongly resembles the alignment reported in the STM- based experiment [80], and shown in Fig.5b, and also that obtained computationally by Rey *et al* [87]. It was stated above that in a recent experiment [81] it was observed that the C_{60} islands predominately nucleated near the HOPG step edges. This result, shown in Fig.6, was based on the scan of a substrate of area $2.2\times3.0\ \mu m^2$ In our simulation, on the other hand, the sizes of our basal planes were, at most, not more than about 25 nm^2. This implies that our substrate terraces represented surface areas in the close proximity of the step edges of the substrate used in the experiment. Hence, we can also state, from our Fig.9d, that the C_{60} film in our simulation nucleated fairly close to the step edge. A larger size system, which would have demanded a far longer period of simulation, would have improved the statistics with respect to the influence of the step edges and the importance of terrace sizes for the film growth.

5.3 Intramolecular features in C_{60}/graphite(0001) system

As we mentioned previously, according to the STM-based experiment of Yu *et al* [82], performed in air, extra structures in the form of bumps and ridges were observed on individual adsorbed molecules. These features had dimensions of 1.6 Å to 2.5 Å and varied from one molecule to the next. According to the experimenters, if these features were indeed real, then they must have originated from electronic states in close proximity to the Fermi energy, E_f, contributing to the STM tunnelling current. However, since a recent calculation [89] had shown that neither the energy of the LUMO level nor that of the HOMO level of C_{60} is close enough to E_f to contribute to the tunnelling current, it was suggested that a probable cause could be *tip-induced* states, since in order to obtain high atomic resolutions, the experiment had to be performed with the tip very close to the sample (about 3.3 Å) where the dominant contribution to the tunnelling current originates from the d_{z^2} state of the d-band metal, W, used as the tip. Very recently we examined this conjecture [85] using the non-equilibrium Green function method of Keldysh [90] for computing the tunnelling current between a W tip, operating in a *constant current* mode, as in the experiment, and one of the absorbed molecules extracted from Fig.9d. Our computations of the STM-like HOMO and LUMO images were based on this method, whose details are described elsewhere [91].

To keep to the experimental imaging conditions as closely as possible, we kept the tip-to-sample separation, i.e., the distance from the apex of the tip to the top of the adsorbed molecule, around 3.3 Å in our computations. Such a small tip-to-sample distance (3.3 Å) in the experiment must have prompted a significant contribution from the d_{z^2} orbital of the apex tip atom to the tunnelling current and must have therefore led to the high resolutions observed in the STM images. However, since the experiment was performed in air, and not under UHV conditions, the contamination of the tip by impurities could not be ruled out and hence the role of the d_{z^2} state of the W tip may not be so clear. Furthermore, we know that [91, 92] artificial features in the STM images, which do not reflect the real charge distribution in the sample, may be generated by a small tip-to-sample separation. Such anomalies may be caused by the tunnelling through those orbitals of the apex atom

in the tip that are oriented parallel to the (x-y) plane, assuming that the z-axis represents the direction perpendicular to the substrate surface. Consequently, for a small tip-to-sample distance and a sufficiently high density of states, tunnelling through these orbitals can produce artificial features in the STM images of the surface, such as an inverted corrugation or the image of an adsorbed atom with a crater-like form [91, 92], neither of which corresponds to the real charge distribution in the sample.

Figs 10 and 11 show respectively the HOMO- and the LUMO-like images of the single adsorbed C_{60} molecule obtained from our computations; the position and orientation of this molecule were obtained from our MD results shown in Fig.9d. In both the HOMO and the LUMO images the positions of the carbon atoms in the upper part of the molecule are marked. We can see that a six-membered ring is approximately parallel to the surface. This is in line with the theoretical calculation [88] where it was found that such a configuration corresponded to the most stable orientation of the C_{60} molecule on the graphite surface irrespective of the position within the surface unit cell.

Detailed analysis of the contributions to the tunnelling current from different orbitals clearly showed that the central regions in both Figs 10 and 11 were mainly built up from the tunnelling through the d_{z^2} orbital of the tungsten tip's apex atom; this contribution constituted around 60% of the total tunnelling current. The perpendicular orientation of the d_{z^2} orbital, with respect to the (x-y) plane, enabled tunnelling from the part of the sample directly located below the tip and therefore we expect that the scanning did correctly reproduce the charge distribution of the C_{60} molecule. In fact, in both Figs 10 and 11 the topographies of the images correspond very well to the charge distribution of the HOMO and the LUMO states of an isolated C_{60} molecule. Our HOMO-like image confirms that the HOMO states were mainly localized on the hexagonal rings. The image also shows the characteristic holes in the centres of the topmost hexagons representing the typical element of the charge distribution of the HOMO states.

The LUMO states of a free C_{60} are located along the single C-C bonds, which make the maxima in the LUMO density of states to appear at the pentagonal rings. This fact is clearly borne out by our numerical results. Fig.11 shows that the dominating features in the central part of our LUMO-like image are located at the three topmost pentagonal rings. Our computed topography compares with the results of calculations of the density of states of the LUMO states of the C_{60} molecule.

The size of the C_{60} molecule in the HOMO- and the LUMO-like images obtained from our computations was larger than its van der Waals diameter, and this is due to the tip-sample convolution effect which is also known experimentally [93]. The tunnelling resistance obtained in our computations was 12 MΩ. This value compares very well with those obtained in the experiment [82] (10 MΩ to 20 MΩ) the examination of whose results was the aim of our computations. This value was, however, much smaller than those obtained in the UHV-based STM experiments, such as [80], where it was found to be about 11 GΩ. This discrepancy must be attributed to the smallness of the tip-to-sample distance employed both in the experiment [82] and our computations where our aim was to test the validity of the claim that the d_{z^2} state of the W tip might have been responsible for the emergence of the extra purported features.

Summarizing the results of our STM-like computations, we can state that our accurate results of the charge distribution of the C_{60} molecule adsorbed on the graphite substrate did not show the presence of any extra states, and this would rule out the possibility that the reported observed intra-molecular features in the experiment [82] originated from the tip-induced states during the scanning process. The structure of these observed features is very different from the topographies of the LUMO or the HOMO-like images of a free C_{60} or a C_{60} physisorbed on the Si(100) or on the Cu(111) surfaces. The origins of these ridges and bumps, if they are indeed real structures and not some experimental anomalies connected with the presence of impurities on the surface or the contamination of the tip by the C_{60} molecules themselves, must be looked for elsewhere, such as the influence of of the graphite substrate.

6. Conclusions

Research into the controlled formation of nano-structured materials in the form of thin films, composed of clusters, adsorbed on varieties of substrates occupies a very central position in experimental nano-scale surface physics and in the newly emerging fields of computational condensed matter physics and materials

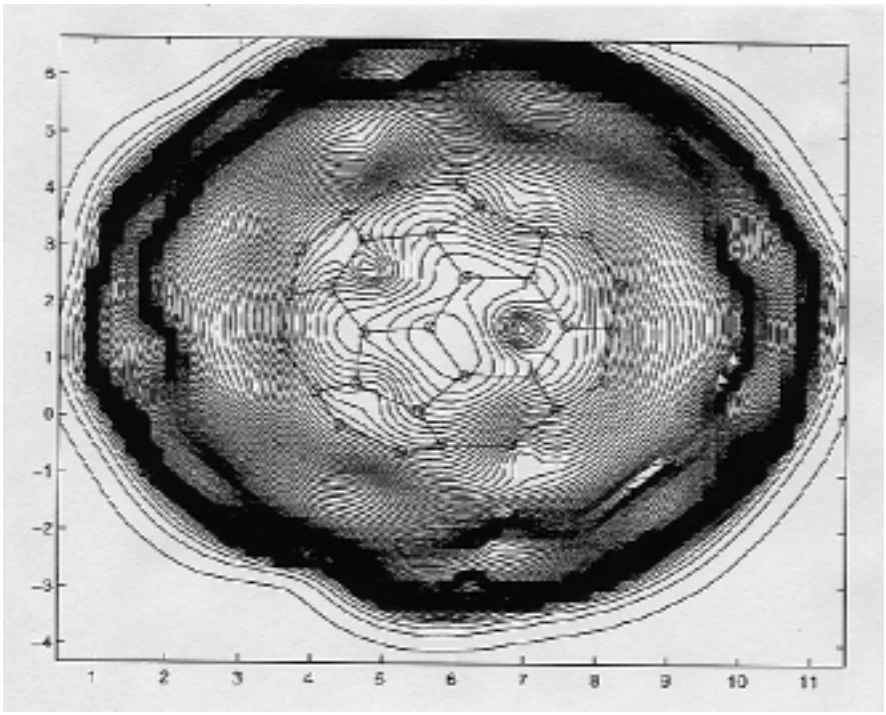

Fig. 10. The computed STM-like image of the HOMO band for a C_{60} molecule extracted from Fig. 9d. The positions of the atoms and the bonds of the top part of the molecule are indicated. The scales are in the units of the nearest neighbour distance between the carbon atoms in an ideal C_{60} molecule, i.e 1.41 $\mathring{A}$. The horizontal and vertical axes refer to the (x, y) coordinates of the tip along the surface.

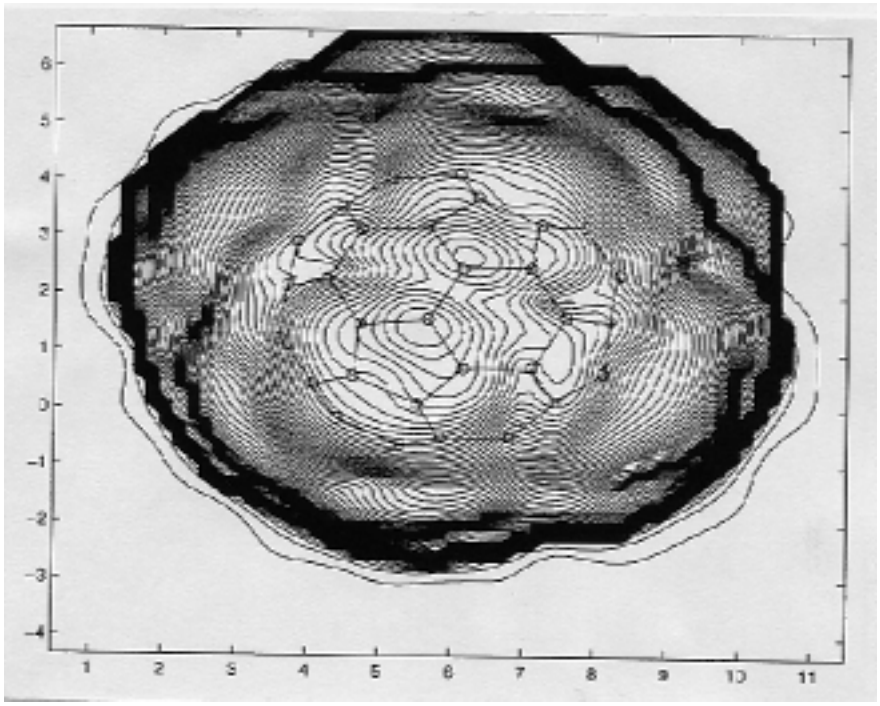

Fig. 11. The computed STM-like image of the LUMO band for a C_{60} molecule extracted from Fig. 9d. The positions of the atoms and the bonds of the top part of the molecule are indicated. The scales and the axes are the same as those in Fig. 10.

modelling. Within this overall framework, an area of deep interest is the growth of nano-scale formations of C_{60} fullerenes on metallic and semi-conducting surfaces. These will have significant applications in quantum-scale device fabrication. In this review, we have surveyed this field both from the experimental and modelling perspectives. The nano-scale modelling studies show the potential power of computer-based simulations to elucidate important problems pertinent to both basic and experimental research that may be beyond the capabilities of the standard macroscopic analytical theories or the experiments. These issues can be very relevant to many research programmes, and in particular to the emerging fields of nano-science and nano-technology. We have seen that our dynamic simulations have been able to predict the experimental results, where they exist. Indeed, since numerical modelling and computer-based simulations can be considered as `computational experimentations', then it is quite possible to use simulations as guides to point to new types of experiments that can be set up, and the range of results that can be expected. These numerical simulations are based on the use of inter-atomic potentials that serve as the physical basis for them. Hence, constructing and testing suitable inter-atomic potentials are an important part of any computational nano-science research programme.

Nano-science and nano-technology are referred to as the `third revolution' in science and technology. There is no doubt that they will come to dominate the sciences and technologies of most countries in the years to come. It is very appropriate that Iran should be involved in this endeavour at this early stage, now that the gap separating the countries involved in the research in these fields is not very wide. One area of research that a country like Iran can be fruitfully involved in is the fullerene-based physics, in projects such as those surveyed in this review.

References

1. K E Drexler, *Nanosystems: Molecular Machinary, Manufacturing and Computation*, Wiley, New York, 1992.
2. Collection of Articles in Science, Vol. **254**, Nov. 1991.
3. http://www.forsight.org.
4. R P Feynman, *Eng. Sci.* **23** (1960).
5. H Gleiter, *Prog. Mater. Sci*. **33** (1989) 223.
6. H Gleiter, *NanoStr. Mater*. **1** (1989) 77.
7. U Erb, *NanoStr. Mater.* **6** (1995) 533.
8. H Rafii-Tabar, *Physics Reports* **325** (2000) 239.
9. G Binnig and H Rohrer, Helv. *Phys. Acta*. **55** (1982) 726.
10. G Binnig, C F Quate and C. Gerber, *Phys. Rev. Lett.* **56** (1986) 933.
11. M P Allen and D J Tildesley, *Computer Simulation of Liquids,* Clarendon Press, Oxford, 1987.
12. J M Haile, *Molecular Dynamics Simulation: Elementary Methods* J. Wiley & Sons Inc, New York, 1992.
13. D C Rapaport, *The Art of Molecular Dynamics Simulation* Cambridge University Press, Cambridge, UK, 1995.
14. R K Pathria, *Statistical Mechanics* Pergamon Press, Oxford, 1972.
15. L V Woodcock, *Chem. Phys. Lett*. **10** (1971) 257.
16. F F Abraham, S W Koch and R C Desi, *Phys. Rev. Lett*. **49** (1982) 923.
17. T Schneider and E Stoll, *Phys. Rev. B***13** (1976) 1216.
18. J M Haile and S Gupta, *J. Chem. Phys*. **79** (1983) 3067.
19. S Nose, *J. Chem. Phys*. 81 (1984) 511.
20. T Schneider and E Stoll, *Phys. Rev. B***17** (1978) 1302.
21. T Schneider and E Stoll, *Phys. Rev. B***18** (1978) 6468.
22. H C Anderson and *J. Chem. Phys*. **72** (1980) 2384.
23. H Tanaka, K Nakanishi and N Watanabe, *J. Chem. Phys.* **78** (1983) 2626.
24. W G Hoover, A J C Ladd and B Moran, *Phys. Rev. Lett.* **48** (1982) 1818.
25. A J C Ladd and W G Hoover, *Phys. Rev. B***28** (1983) 1756.
26. D J Evans and *J. Chem. Phys*. **78** (1983) 3297.
27. H J C Berendsen, J P M Postma, W F van Gunsteren, A DiNola and J R Haak, *J. Chem. Phys.* **81** (1984) 3684.
28. S Nose', *Mol. Phys*. **52** (1984) 255.
29. S Nose', *Prog. Theor. Phys. Suppl*. **103** (1991) 1.
30. W G Hoover, *Phys. Rev. A***31** (1985) 1695.
31. J Jellinek and R S Berry, *Phys. Rev. A***38** (1988) 3069.

32. A P Sutton, J B Pethica, H Rafii-Tabar and J A Nieminen, in: D G Pettifor, A H Cottrell (Eds.), *Electron Theory in Alloy Design*, Institute of Materials, London, 1994, p. 191.
33. S Erkoc, *Physics Reports* **278** (1997) 79.
34. G C Abell, *Phys. Rev. B***31** (1985) 6184.
35. J Tersoff, *Phys. Rev. Lett*. **56** (1986) 632.
36. J Tersoff, *Phys. Rev. B***37** (1988) 6991.
37. J Tersoff, *Phys. Rev. B***38** (1988) 9902.
38. J Tersoff, *Phys. Rev. Lett*. **61** (1988) 2879.
39. J Tersoff, *Phys. Rev. B***39** (1989) 5566.
40. D W Brenner, *Phys. Rev. B***42** (1990) 9458.
41. D W Brenner, S B Sinnott and J A Harrison, private communication.
42. dwb@ripley.mte.ncsu.edu.
43. K Dharamvir and V K Jindal, *Int. J. Mod. Phys. B***6** (1992) 281.
44. R S Ruoff and A P Hickman, *J. Phys. Chem*. **97** (1993) 2494.
45. Cheng and M L Klein, *Phys. Rev. B***45** (1992) 1889.
46. W A Steele, *The Interaction of Gases with Solid Surfaces*, Pergamon, New York, 1974.
47. L A Girifalco, *J. Chem. Phys*. **96** (1992) 858.
48. J A Venables, G D T Spiller and M Hanbücken, *Rep. Prog. Phys*. **47** (1984) 399.
49. H W Kroto, J R Heath, S C O'Brian, R F Curl and R E Smalley, *Nature* **318** (1985) 162.
50. W Kratschmer, L D Lam, K Fostiropoulos and D R Huffman, *Nature* **347** (1990) 354.
51. M Terrones, W K Hsu, J P Hare, H W Kroto, H Terrones and D R M Walton, *Phil. Trans. R. Soc. (Lond) A***354** (1996) 2025.
52. C S Yannoni, R D Johnson, G Meijer, D S Bethune and J R Salem, *J. Phys. Chem*. **95** (1991) 9.
53. S Saito and A Oshiyama, *Phys. Rev. Lett*. **66** (1991) 2637.
54. M S Dresselhaus, G Dresselhaus, and P C Eklund, in: *Sience of Fullerenes and Carbon Nanotubes,* Academic Press, San Diego, 1996, p.172.
55. P A Heiney, J E Fisher, A R McGhie, W J Ropmanow, A M Denestein, J P Mc-Cauley Jr, A B Smith III and D E Cox, *Phys. Rev. Lett*. **66** (1991) 2911.
56. K Tanigaki, T T Ebbesen, S Saito, J Mizuki, J S Tsai, Y Kubo and S Kuroshima, *Nature* **352** (1991) 222.
57. R J Wilson, G Meijer, D S Bethune, R D Johnson, D D Chambis, M S de Vries, H E Hunziker and H R Wendt, *Nature* **348** (1990) 621.
58. L D Lamb, D R Huffman, R K Workman, S Howells, T Chen, D Sarid and F Ziolo, *Science* **255** (1992) 1413.
59. E I Altman and R J Colton, *Surf. Science* **279** (1992) 49.
60. E I Altman and R J Colton, *Phys. Rev B***48** (1993) 244.
61. Y Kuk, D K Kim, Y D Suh, K H Park, H P Noh, J S Oh and S K Kim, *Phys. Rev. Lett*. **70** (1993) 1948.
62. E I Altman and R J Colton Surf. *Sci.* **295** (1993) 13.
63. J K Gimzewski, S Modesti and R R Schlittler, *Phys. Rev. Lett*. **72** (1994) 1036.
64. J K Gimzewski, S Modesti, T David and R R Schlittler, *J. Vac.Sci. Technol. B***12** (1994) 1942.
65. K Motai, T Hashizume, H Shinohara, Y Saito, H W Pickering, Y Nishina and T Sakurai, *Jpn. J. Appl. Phys*. **32** (1993) L150.
66. M R C Hunt, S Modesti, P Rudolf and R E Palmer, *Phys. Rev. B***51** (1995) 10039.
67. A J Maxwell, P A Bruhwiler, A Nilsson, N Martensson and P Rudolf, *Phys. Rev B***49** (1994) 10717.
68. X-D Wang, T Hashizume and T Sakurai, *Mod. Phys. Lett*. *B***8** (1992) 1597.
69. Y Maruyama, K Ohno and Y Kawazoe, *Phys. Rev. B***52** (1995) 2070.
70. C K Ong and B C Chan, *J. Phys.: Condens Matter* **1** (1989) 3931.
71. Y Z Li, M Chander, J C Partin, J H Weaver, L P F Chibante and R E Smalley, *Phys. Rev. B***45** (1992) 13837.
72. X-D Wang, T Hashizume, H Shinohara, Y Saito, Y Nishina and T Sakurai, *Jpn J. Appl. Phys*. **31** (1992) L983.
73. T Hashezume, X-D Wang, Y Nishina, H Shinohara, Y Saito, Y Kuk and T Sakurai, *Jpn. J. Appl. Phys*. **31** (1992) L880.
74. T Hashezume, X-D Wang, Y Nishina, H Shinohara, Y Saito, Y Kuk and T Sakurai, *Jpn. J. Appl. Phys*. **32** (1993) 15923.
75. X-D Wang, T Hashizume, H Shinohara, Y Saito, Y Nishina and T Sakurai, *Phys. Rev. B***47** (1993) 165.
76. Y Z Li, J C Partin, M Chande, J H Weaver, L P F Chibante and R E Smalley, *Science* **252** (1991) 547.

77. M R C Hunt and R E Palmer, *Surf. Rev. Lett*. **3** (1996) 937.
78. M F Luo, Z Y Li and W Alison, *Surf. Sci*. **437** (1998) 402-404.
79. S Suto, A Kasuya, C-W Hu, A Wawro, T Goto and Y Nishina, *Surf. Rev. Lett*. **3** (1996) 927.
80. S Suto, A Kasuya, C-W Hu, A Wawro, T Goto and Y Nishina, *Thin Solid Films* **602** (1996) 281-282.
81. D J Kenny and R E Palmer, *Surf. Sci.* **447** (2000) 126.
82. H Yu, J Yan, Y Li, W S Yang, Z Gu and Y Wu, *Surf. Sci*. **286** (1993) 116.
83. H Rafii-Tabar, H Kamiyama, Y Maruyama, K Ohno and Y Kawazoe, *Mol. Simul*. **12** (1994) 271.
84. H Rafii-Tabar, A L TambyRajah, H Kamiyama and Y Kawazoe, *Model. Simul. Mater. Sci. Eng.* **4** (1996) 101.
85. H Rafii-Tabar, L Jurczyszyn and B Stankiewicz, *J. Phys.: Cond Matt.* **12** (2000) 5551.
86. R Car and M Parrinello, *Phys. Rev. Lett*. **55** (1985) 2471.
87. Rey, J Garcia-Rodeja, L J Gallego and J A Alonso, *Phys. Rev. B***55** (1997) 7190.
88. P A Gravil, M Devel, Ph Lambin, X Bouju, Ch Girard and A A Lucas, *Phys. Rev. B***53** (1996) 1622.
89. R C Haddon, L E Burs and K Raghavachari, *Chem. Phys. Lett*. **125** (1986) 459.
90. L V Keldysh, Zh Eksp, *Teor.Phys*. **47** (1964) 1515; *Sov. Phys. JETP* **20** (1965) 1018.
91. N Mingo, L Jurczyszyn, F J Garcia-Vidal, R Saiz-Pardo, P L de Andres, F Flores, S Y Wu and W More, *Phys. Rev. B***54** (1996) 2225.
92. F Flores, P L de Andres, F J Garcie-Vidal, L Jurczyszyn, N Mingo and R Perez, *Prog. Surf. Sci.* **48** (1995) 27.
93. X Yao, T G Ruskell, R K Workmann, D Sarid and D Chen, *Surf. Sci.* **367** (1996) L85.